J. Fluid Mech. (1991), *vol.* 228, *pp.* 25–51
Printed in Great Britain

The velocity and vorticity vector fields of a turbulent boundary layer. Part 1. Simultaneous measurement by hot-wire anemometry

By PETAR VUKOSLAVČEVIĆ,† JAMES M. WALLACE AND JEAN-LOUIS BALINT

Department of Mechanical Engineering, The University of Maryland, College Park, MD 20742, USA

(Received 12 January 1990 and in revised form 14 December 1900)

A nine-sensor hot-wire probe is described which is capable of simultaneously measuring the velocity and vorticity vectors with a spatial resolution of about six Kolmogorov microscales just above the viscous sublayer in a thick turbulent boundary layer at a Reynolds number of $R_\theta = 2685$. Results from tests of the probe performance are presented to show that the three velocity components at each of its three arrays are measured with sufficient accuracy to allow determination of velocity gradients and from them the vorticity vector. Measurements with this probe of statistical properties of the velocity and vorticity fields of the turbulent boundary layer are given in Part 2 of this paper. When compared to the results of others, they further demonstrate the capability of this probe to measure simultaneously the velocity and vorticity vectors in turbulent flows of low to moderate Reynolds numbers.

1. Introduction

The measurement of one or more components of the vorticity vector

$$\Omega_i = \epsilon_{ijk} \frac{\partial U_k}{\partial x_j}, \tag{1}$$

where ϵ_{ijk} is the alternating tensor and U_k is the velocity vector, has long been an elusive goal of experimental turbulence research. The importance of such measurements is rather obvious. Vorticity is a defining property of turbulence; the presence of vorticity in a flow is deemed essential to identifying it as truly turbulent motion. More than three decades ago, for example, Corrsin & Kistler (1954), analysed the properties of the frontier, which they named the viscous superlayer, sharply delineating irrotational or non-vortical motion in the free stream of turbulent shear flows from the rotational or vortical motion in their interiors. The experimental study of the entrainment process at this frontier has been impeded by the absence of a method to detect accurately the frontier. The organized motions in shear flows, which have been so intensively studied over the past twenty-five years, are for the most part vortical motions. The lack of experimental means to measure vorticity also has impeded their study. Furthermore, there are other advantages to describing the

† On leave from the Veljko Vlahović University, 81000 Titograd, Yugoslavia.

dynamics of turbulent motion in terms of vorticity. The equation of motion in vorticity form,

$$\frac{\partial \Omega_i}{\partial t} + U_j \frac{\partial \Omega_i}{\partial x_j} = \Omega_j \frac{\partial U_i}{\partial x_j} + \nu \frac{\partial^2 \Omega_i}{\partial x_j \partial x_j}, \tag{2}$$

in contrast to the Navier–Stokes equation describing momentum transport, does not directly include pressure, which allows some simplification in computation and interpretation. Moreover, the vorticity form for expressing the flow dynamics is much more amenable to experiments, because pressure measurements within the flow have proven to be even more difficult than vorticity measurements.

Much insight was gained about turbulence dynamics from measurements of the balance of terms in the transport equations for kinetic energy made by Townsend (1951), Laufer (1953) and Klebanoff (1954), which are now considered classic. Further understanding of these dynamical processes will surely be gained from knowledge of the balance of terms in the analogous transport equation for total enstrophy $\frac{1}{2}\Omega_i^2$, which is a scalar measure of the magnitude of vortical activity. Measurements of the balance of these enstrophy terms in a turbulent boundary layer will be reported in Part 2 of this paper (Balint, Wallace & Vukoslavčević 1991).

After reviewing other hot-wire methods available to measure one or more components of the vorticity vector in the next section, the rest of Part 1 will describe the construction, calibration and testing of a miniature multi-sensor hot-wire probe. This probe utilizes a particular geometric arrangement of nine sensors to obtain measurements of all three components of the vorticity vector simultaneously with all three components of the velocity vector in turbulent flow. Moreover, the velocity measurements account for the non-uniformity of the turbulent flow field across the sensing area of the probe. This accounting for the effect of instantaneous velocity gradients on velocity measurements with hot wires has never previously been done, to the authors' knowledge. It will be shown that it requires a minimum of nine sensors. Those who wish a more detailed description of the operation of this probe can refer to Vukoslavčević, Wallace & Balint (1990). Part 2 will report many properties of both the velocity and vorticity vector fields simultaneously measured with this probe in a turbulent boundary layer at $R_\theta = 2685$, where θ is the momentum thickness. Conditionally averaged properties of the boundary layer obtained from further analysis of this database will be described in a later paper. The probe has also recently been utilized in a two-stream turbulent mixing layer, in a turbulent grid flow and in an axisymmetric turbulent jet.

2. Previous measurements of vorticity components with hot-wire anemometry

These measurements all require an accurate estimate of velocity components at closely spaced points in the flow from which vorticity components are obtained by determining the circulation around a small planar area or, alternatively, by determining the velocity gradients by finite difference. As the spatial distance between the velocity measurement locations is reduced, the two methods are indistinguishable. With the circulation method, as the circuit becomes larger, the measured spatial average vorticity in the circulation plane obviously becomes an increasingly poorer estimate of the instantaneous vorticity at the centre of the plane. A finite-difference approximation of the gradients, on the other hand, assumes that second- and higher-order terms are negligible in a Taylor expansion of the velocity

field about the measurement point in the flow. This assumption obviously also becomes increasingly less valid as the spatial distance over which the gradients are estimated increases.

Complete surveys of these previous hot-wire vorticity component measurements as well as measurements which directly sense vorticity or velocity gradients have been given by Wallace (1986) and by Foss & Wallace (1989). Here we will summarize only briefly the hot-wire methods.

2.1. *Streamwise vorticity*

Kovasznay (1950, 1954) proposed an arrangement of four hot-wire sensors, which act as the four legs of a Wheatstone bridge, in order to measure Ω_x. Kistler (1952) analysed the operation of this probe and used it to measure the one-dimensional vorticity spectrum and its decay in a turbulent grid flow. Corrsin & Kistler (1954) measured the r.m.s. streamwise vorticity distribution in a roughened boundary layer with a probe of this design; Tu and Willmarth also made turbulent-boundary-layer measurements with a Kovasznay-type probe (see Willmarth & Lu 1972), but with very poor spatial resolution. Kastrinakis (1976) used two Kovasznay-type probes to measure the r.m.s. distribution of streamwise vorticity across a fully developed turbulent channel flow as well as the two-point correlation coefficient for spanwise probe separation. Kastrinakis *et al.* (1977) used the same two probes to investigate wall-layer vortical structures. Kastrinakis, Eckelmann & Willmarth (1979) showed that there is a very considerable parasitic sensitivity of values of Ω_x, as measured by the Kovasznay-type probe, to the streamwise and cross-stream velocity components. This analysis confirmed what Kistler (1952) had implied. They found that contamination by the cross-stream velocity, which increases with mean velocity, can be of the same order as that of the instantaneous vorticity to be measured in many turbulent flows.

Vukoslavčević & Wallace (1981) built and analysed a probe with the same geometric arrangement as a Kovasznay-type, but with each wire operated independently as had been proposed by Kastrinakis *et al.* (1979). This modified Kovasznay-type probe has two pairs of sensors forming two orthogonal X-arrays which, if the conventional assumption of uniform velocity across the probe measuring area is made, yields three velocity components as well as the streamwise vorticity. Of course the disadvantage is that this design requires twice as many supporting prongs as the original Kovasznay design. Although it would seem that the parasitic contamination of Ω_x by the velocity components then could be corrected, Vukoslavčević & Wallace (1981) emphatically stress that *this necessary assumption of uniform flow across the sensing area of this and other multi-sensor hot-wire arrays (including simple X-array probes) is invalid in highly turbulent flows.* Large internal shear layers often are present instantaneously which contaminate the measurement of V and W themselves. This assertion is supported by their measurements of the maximum values of $\partial U/\partial y$ and $\partial U/\partial z$ in a boundary layer. The presumed presence of these large-amplitude, small-scale internal shear layers had previously been assumed by Willmarth & Bogar (1977) to explain anomalies in a boundary-layer data at $y^+ = 3$ measured with a very small X-array hot-wire probe (wire length and spacing of 0.1 mm or 2.5 viscous lengths at $R_\theta = 11700$). These authors speculated that each of the sensors responded to a quite different velocity vector, thereby contradicting the necessary assumption of uniform flow across the sensing area for the formulation of the response equations.

Vukoslavčević & Wallace (1981) in essence then made explicit the implicit and

rather implausible assumption inherent in the design of both the original and the modified Kovasznay-type probes, i.e. that these probes are only sensitive to the velocity gradients of the streamwise vorticity component but are not sensitive to the other four velocity gradients in the cross-stream plane. This modified version of the Kovasznay-type probe thus also can yield quite erroneous instantaneous values of $\Omega_x(t)$. The discovery of this instrumentation problem in attempting to measure streamwise vorticity using hot-wire anemometry was our initial motivation for using nine sensors in order to estimate all the velocity gradients and thus to account for the non-uniformity of the flow over the probe sensing area.

Some of the basic statistics of the streamwise vorticity in a turbulent channel flow were measured by Kastrinakis & Eckelmann (1983) using this modified Kovasznay-type probe with a resolution of about 11.5 viscous lengths or about 6.5 times their estimation of the Kolmogorov microscale in the buffer layer. The V and W velocity components were systematically underestimated by about 20% when the probe was tested by pitching and yawing it in a uniform irrotational flow. Empirically determined calibration factors were therefore necessary to correct their data measured in the turbulent flow. Kastrinakis, Nychas & Eckelmann (1983) examined the percentage contributions to the mean-square streamwise vorticity component conditioned on the quadrant analysis of the uv product time series with this same probe. The autocorrelations of the streamwise vorticity fluctuation ω_x were obtained for positions across the channel, and from these the corresponding integral lengthscales for ω_x and ω_x^2 were determined. These data were later used by Nychas, Kastrinakis & Eckelmann (1985) to estimate components of the production and dissipation rate terms in the fluctuating enstrophy transport equation.

2.2. *Cross-stream vorticity*

An array of four hot-wire sensors to measure the transverse vorticity component Ω_z in turbulent flows has been developed by Foss and his co-workers (Foss 1981; Foss, Ali & Haw 1987). Foss *et al.* (1987) have studied many of the operating attributes of this probe and find that the most important problem is that due to the non-uniformity of the flow in the spanwise direction, confirming the conclusion of Vukoslavčević & Wallace (1981) mentioned earlier. Measurements of the velocity fluctuations u and v, the spanwise vorticity fluctuation ω_z, and the strain rate component ϵ_{xy} at the entraining boundary of a large plane shear layer have been made by Foss, Klewicki & Disimile (1986) using a probe of this design. This type probe was also used by Falco (1983) to obtain ensemble averages of the spanwise vorticity in a smoke-marked turbulent boundary layer. Klewicki & Falco (1990) have recently used it to measure the statistics of the spanwise vorticity component at $R_\theta = 1010$–4850 in a boundary layer with a 2.56–0.64 mm thick sublayer over this Reynolds-number range. A new design reduces the spanwise gradient error, and results obtained with this new design have been presented by Haw, Foss & Foss (1989).

A five-sensor hot-film probe for the measurement of both the spanwise and normal components of vorticity was used by Eckelmann *et al.* (1977). Although they were able to obtain ensemble-average patterns of these two vorticity components utilizing the pattern recognition algorithm of Wallace, Brodkey & Eckelmann (1977), for $y^+ > 10$ they were not able to measure accurately and directly the mean velocity gradient $\partial\bar{U}/\partial y$ by taking instantaneous U velocity component differences in the y-direction over the approximately one Kolmogorov-length sensor separation. It was later shown by Böttcher & Eckelmann (1985) that direct measurement of the mean

velocity gradient is very difficult to obtain accurately because of probe interference of the flow field.

The normal and spanwise vorticity fluctuation components ω_y and ω_z of a turbulent wake have been measured, but not simultaneously, by Antonia, Browne & Shah (1988) with two hot-wire X-arrays separated in the appropriate cross-stream direction by 1.6 mm and utilizing Taylor's hypothesis. The spacing between the wires of each array was 1 mm; the Kolmogorov microscale for this flow, estimated from the average isotropic dissipation, was found to be about 0.45 mm at the centreline.

Recently Kim & Fiedler (1989) have designed and used a six-sensor probe to determine ω_z and ω_x. Their measurements of the standard deviation of the transverse vorticity component in a two-stream mixing layer show good agreement with the LDV measurements of Lang (1985).

2.3. *The three components of vorticity measured simultaneously*

Besides the nine-sensor hot-wire probe method of measuring all the components of the vorticity vector which is the principal subject of this paper, there are only a few other methods which attempt to measure all three components of the vorticity vector simultaneously, and none of them utilize hot-wire anemometry. As discussed in Foss & Wallace (1989), to date none of these other methods have operated successfully in turbulent flows.

Although this section is a brief review of existing hot-wire anemometry methods for measuring vorticity, it should be noted that methods using direct numerical simulations of the Navier–Stokes equation have been developed which determine the vorticity vector over the entire flow field. Although these numerical methods are presently limited to low Reynolds numbers and simple geometries, they have provided the full three-dimensional velocity and vorticity vector fields for fully developed channel flow (Kim, Moin & Moser 1987), for the turbulent boundary layer at R_θ up to 1410 (Spalart 1988), for homogeneous turbulent shear flow and various irrotational straining flows (Rogers & Moin 1987), and for the temporally evolving plane mixing layer (Metcalfe *et al.* 1987). In Part 2 we will compare some of the results obtained from these simulations with our laboratory measurements and those of others.

3. The nine-sensor hot-wire probe

3.1. *Design and construction*

The probe consists of three arrays of three hot-wire sensors oriented at 45° to the mean flow as seen in the top, side and end view photographs of figure 1 (*a–c*) and in the schematic drawing of the supporting prongs and hot-wire arrangement of figure 1 (*d*). The total dimensions of the probe sensing area are 1.7 mm vertically and 2.2 mm horizontally with an average distance between the sensor centres of about 1.2 mm, and a distance h between the supporting prongs of any array of 0.5 mm. The diameter of the nine tungsten sensors is 2.5 μm and their length is about 0.7 mm, giving a length-to-diameter ratio of 280. The probe could easily be made half this size; however, the spatial resolution requirements of the probe must be balanced by other requirements which affect measurement accuracy. The velocity and vorticity measurement accuracy can, of course, increase with decreased array spacing to the extent that the neglected second- and higher-order terms in the Taylor series expansion of the velocity at the probe centroid, as described in §4, are important

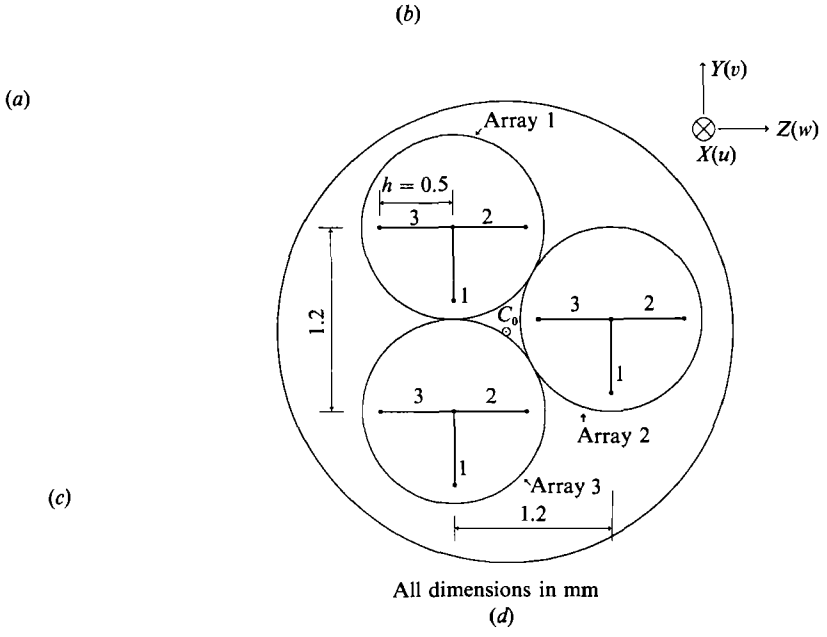

FIGURE 1. (a) Top view photograph of the probe, (b) side view photograph, (c) end view photograph; (d) end view schematic.

over this distance. Their neglect obviously makes the estimate of velocity gradients by first-order finite difference less accurate. On the other hand, this measurement accuracy will decrease as the spacing between arrays is reduced for two reasons. First, the relative accuracy of velocity difference measurements decreases as the values of the two velocities to be differenced become close to each other. This is because the absolute accuracy of each velocity measurement is independent of spatial separation to the extent that the first-order gradient approximation is nearly valid. Second, the relative accuracy of the estimation of the spacing between arrays (the denominator in the first-order velocity gradient estimate) also decreases with decreased spacing by the same reasoning. In addition, the effects of aerodynamic and thermal interference of these closely spaced prongs and wires must be considered, as will be discussed in §5.4. All these competing considerations must be balanced in the choice of sensor lengths and spacings.

Fabrication of the probe is difficult because of its small size, complex design and fragility. The main problem is to fit twelve supporting prongs in the smallest feasible space while still satisfying accuracy as well as resolution criteria. Arranging the prongs with very small distances between them presents two difficult problems: preventing electrical shorts between the prongs or between the prongs and the probe

body, and maintaining the prongs in place so that they keep the desired array geometry. Several technical solutions and various prong materials have been tried. The latest version of the probe uses nickel-plated tungsten wire of about 0.25 mm diameter for supporting prongs. Short pieces of this wire are tapered from their original diameter to a tip diameter of about 0.075 mm by burning them with a micro-torch and filing them with emery cloth. The four prongs of each array are then drawn through round 4-bore ceramic insulating tubes. These tubes have an outside diameter of about 1.6 mm and each hole has a diameter of about 0.3 mm. The three ceramic tubes are then placed in a stainless steel tube of about 4.8 mm outside diameter with one flat side in order to bring the probe as close as possible to the wall. The prong tips are manipulated under a measuring microscope into their proper geometric position within about a 0.01 mm tolerance and are epoxyed together at one end of the ceramic tubes. Insulated lead wires and miniature plug connectors are soldered to the other ends. The ceramic tubes are then sealed into the outer stainless steel tube with epoxy. A photograph of the entire probe assembly is shown in figure 2. After nickel plating the prong tips and electro-cleaning the sensor wire, the 2.5 μm diameter, unsheathed, tungsten wire sensors are welded to the tips with a condenser storage micro-welding device. When the welding of all nine sensors is complete, the probe tip is submerged in the nickel plating solution and the sensors and prong tips are plated together for a further short period. This makes the probe structurally much more robust while only reducing the sensor resistances by about 10%.

3.2. *Spatial resolution of the probe*

The choice of the probe dimensions described above has been guided by two resolution criteria which both need to be satisfied as well as possible consistent with the accuracy requirement. In order to estimate with good resolution the velocity effectively cooling each sensor, each sensor length should be smaller than the size of the smallest turbulent structure encountered in the flow, i.e. the Kolmogorov microscale η. The previously reported estimate of our probe resolution by Balint, Vukoslavčević & Wallace (1987) was obtained from a scaling argument of Tennekes & Lumley (1972) which assumes, among other things, that production equals dissipation rate in the logarithmic layer. This estimate gives a value of $\eta = 0.165$ mm at $y^+ = 11.2$ (our measurement location closest to the wall) for the nominally zero-pressure-gradient boundary layer described in Part 2. However, the assumptions underlying this estimate do not hold well at this location, as will be seen in Part 2. Using our directly measured values of the dissipation rate, which compare well to direct numerical simulation values as reported in Part 2, we find that $\eta = 0.192$ mm at $y^+ = 11.2$. Thus the sensor lengths are about 3.6 times the measured Kolmogorov microscale at this R_θ for our measurement location closest to the wall. For positions further from the wall, η becomes larger as the kinetic energy dissipation rate ϵ becomes smaller, giving better sensor resolution. Clearly the sensors do not resolve the very smallest turbulence scales, as is the case for virtually all turbulence measurements.

In order to test the effects of these small scales on our velocity measurements with the nine-sensor probe, we built a very small single-sensor probe with a wire length of about 0.3 mm, i.e. about 1.6η. This probe was calibrated and then used to measure the one-dimensional frequency spectrum $\phi_u(f)$ of the streamwise velocity component at $y^+ \approx 18$ in the boundary layer at the same R_θ as in the nine-sensor probe experiment. This spectrum is compared to that obtained with the nine-sensor probe in figure 3. The agreement between the two spectra is excellent with only a small

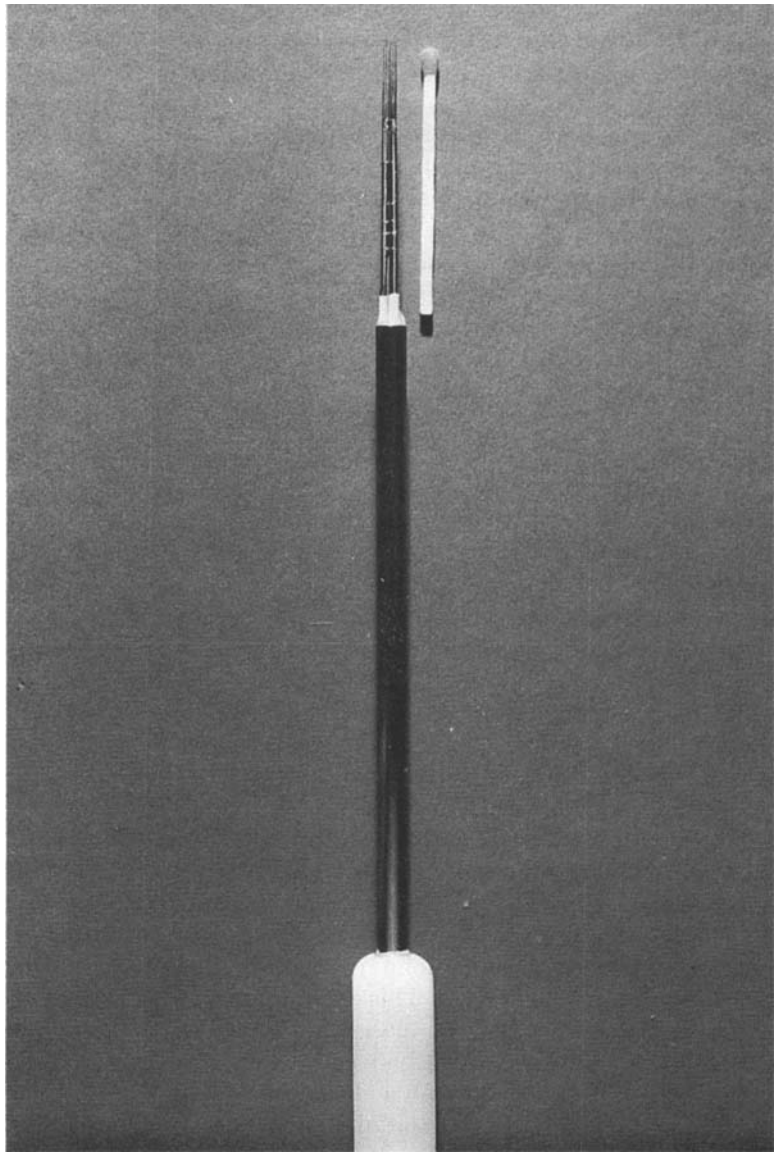

FIGURE 2. Photograph of the probe assembly.

difference at the higher frequencies where the contribution to the energy is two decades below the maximum. Additionally, it will be seen in Part 2 that our streamwise and normal velocity component spectra compare quite well with those of Wei & Willmarth (1989) whose LDV measurements resolved the velocity field within 2.2 Kolmogorov scales in all directions at $y^+ = 15.9$.

The probe should also be able to resolve adequately the velocity gradient field in the flow. A measure of this resolution criterion is the average spacing between sensor centres over which gradients are estimated. This average spacing for this probe is about 6.3 Kolmogorov microscales (or 10.9 viscous lengths) at $y^+ = 11.2$ in the boundary-layer flow described above. The resolution of a Kovasznay-type vorticity probe has been theoretically investigated by Wyngaard (1969) assuming isotropy

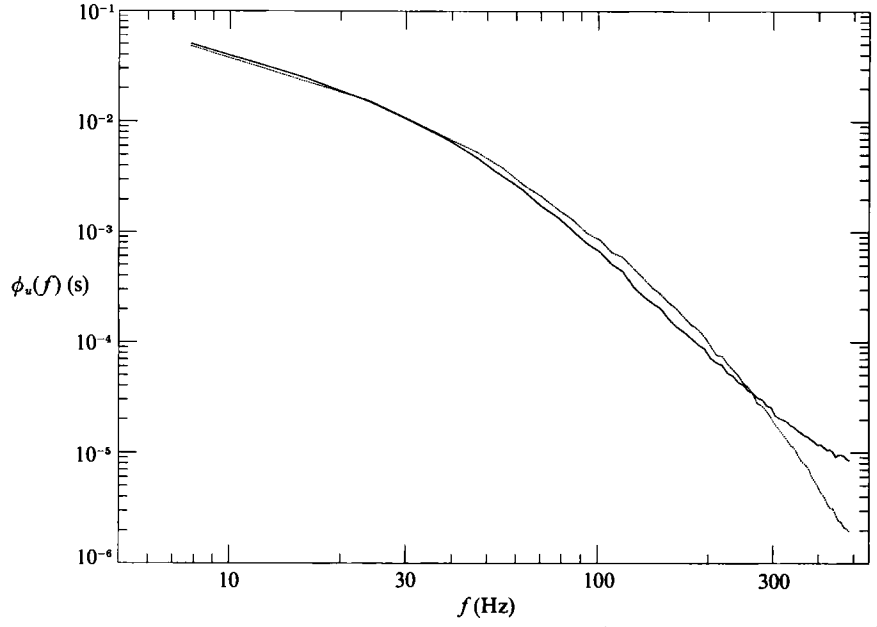

FIGURE 3. Comparison of streamwise velocity component frequency spectra obtained with single-sensor (dotted line) and nine-sensor (solid line) probes measured at $y^+ \approx 18$. Sensor lengths for the two probes are 1.6 and 3.6 Kolmogorov lengths respectively.

and a form of the three-dimensional velocity spectrum given by Pao (1965). He concludes that a reasonable design goal for η/l, where l is the active sensor length, is about 0.3 (for d/l of about 0.7, where d is the spacing between adjacent support prongs). With these dimensions, he estimates that the Kovasznay-type probe measures about 86% of the true mean-square value of the vorticity. For the nine-sensor probe at $y^+ = 11.2$ in the boundary layer described above, $\eta/l = 0.27$. The rough equivalent of d/l for the nine-sensor probe is the ratio of the average spacing between sensor centres to the length of the sensors, which is about 1.7. Wyngaard (1969) shows that additional attenuation of the vorticity spectrum occurs for $d/l > 0.7$. He also analysed, with the assumptions mentioned above, the resolution of velocity gradient measurements made with two parallel hot wires. For $\eta/l = 0.27$ and $d/l = 1.7$, the measured mean-square gradient is about 65% of the true value. As Wyngaard (1969) makes clear however, this analysis should only be used as a design guide because the assumptions in his analysis do not completely hold for a boundary layer near the wall. Klewicki & Falco (1990) have recently obtained experimental support for this analysis, even in the anisotropic conditions of the boundary layer, with measurements of the r.m.s. velocity gradient $\mathrm{d}u/\mathrm{d}y$ made with two parallel sensors with variable separation. They estimate that the previous version of our probe (Balint *et al.* 1987) only attenuates the r.m.s. ω_z measurement by about 10–15% at $R_\theta = 2100$. Furthermore, when we compare our vorticity component spectra to those of P. R. Spalart (1990 private communication) in Part 2, it will be seen that they agree very well except at Spalart's highest wavenumbers where his spectra show some evidence of aliasing. Spalart's direct simulation resolved the vorticity field to within about 11.2, 1.2 and 3.8 Kolmogorov scales in the x-, y- and z-directions respectively at $y^+ = 15$.

From all these considerations, then, it seems reasonable to conclude that, for the measurements described in Part 2, the nine-sensor probe is able to resolve all but the

smallest turbulent scales in the thick turbulent boundary layer used in this study. A complete comparison with the spatial resolution of other laboratory and simulation methods is tabulated in Part 2.

4. Equations governing the operation of the vorticity probe

For multi-sensor probes with their sensors inclined to the mean flow, one of the possibilities for expressing the effective cooling velocity U_e is

$$U_e^2 = U_{N_1}^2 + k_T^2 U_T^2 + k_b U_{N_2}^2, \tag{3}$$

where U_{N_1} is the velocity component normal to the sensor in the plane of its supporting prongs, U_T is the component tangent to the sensor in this plane, and U_{N_2}, often called the binormal component, is the component normal to the sensor in the plane normal to the plane of the prongs. The coefficient k_b takes into account, among other unknown effects, the aerodynamic blockage resulting from the size and arrangement of sensors and prongs; its value is usually somewhat greater than 1.0 because the fluid accelerates when passing through the prongs. The effective cooling velocity can be related to the measured voltage by King's (1914) law.

The coefficient k_T varies from about 0.2 for $l/d = 200$ to about zero for $l/d = 600$ (Champagne, Sleicher & Wehrmann 1967). For the nine-sensor probe, the ratio $l/d = 280$ requires that tangential cooling should be taken into account. A good way of doing this as well as accounting for other effects is the concept of an 'effective' sensor angle α_e introduced by Bradshaw (1975) and used by Bruun & Tropea (1980). For a velocity vector inclined to the direction of the probe axis in the (x, y)-plane of figure 1 (d),

$$U_N = U\cos\alpha + V\sin\alpha \tag{4}$$

for sensors in this plane. U is the velocity component in the x-direction, V is the component in the y-direction, and α is the angle formed by the probe axis (x-direction) and the normal to the sensor in the (x, y)-plane. Similar expressions can be written for the sensors in the (y, z)-plane. Expression (4) for U_N requires that the actual value of the angle α be known with high accuracy. For multi-sensor probes, even with extreme care in the probe construction, sensor angles which are not exactly equal to their ideal values will usually occur. Moreover, it is very difficult to get a good measurement of these angles. However, introducing an effective angle to be determined from calibration in the expression for the normal velocity U_N will circumvent those problems and take into account combined effects such as tangential cooling, probe configuration asymmetry, some aerodynamic blockage, and possible thermal contamination due to some sensors being affected by the thermal wake of others. Hereafter we will use the effective angle α_e in order to define the effective cooling velocity

$$U_e^2 = (U\cos\alpha_e + V\sin\alpha_e)^2 + k_b W^2 \tag{5}$$

for the sensors in the (x, y)-plane of figure 1 (d), with similar expressions written for the sensors in the (x, z)-plane.

We can define the effective cooling velocity $U_{e_{ij}}$ on sensor j of array i of the nine-sensor probe in terms of the velocity components U_0, V_0, W_0 at the centre of the probe C_0 (see figure 1 d) and their gradients in the plane normal to the probe axis passing through the sensor centres, the distance projected on this plane h between the prong tips of any array, the individual sensor effective angle $\alpha_{e_{ij}}$, and the blockage coefficient of sensor j of array i ($i = 1, 2, 3$; $j = 1, 2, 3$). The velocity components U_0, V_0, W_0 are

expanded to first order in a Taylor series about C_0, thus giving the following set of nine nonlinear algebraic equations in nine velocity and cross-stream velocity gradient component unknowns:

$$(U_{e_{ij}})^2 = \left[K_{ij1}\left(U_0 + C_{ij1}\frac{\partial U}{\partial z} + C_{ij2}\frac{\partial U}{\partial y}\right) + K_{ij2}\left(V_0 + C_{ij3}\frac{\partial V}{\partial z} + C_{ij4}\frac{\partial V}{\partial y}\right)\right]^2 + K_{ij3}\left(W_0 + C_{ij5}\frac{\partial W}{\partial z} + C_{ij6}\frac{\partial W}{\partial y}\right)^2. \quad (6)$$

It is therefore clear that nine sensors are required in order to account to first order for the non-uniformity of the velocity field across the probe in this plane. In these equations V is interchanged with W for $j = 2$ and 3. The 27 K_{ijk} coefficients are determined from calibration. The K_{ij1} coefficients are cosines of the effective angles $\alpha_{e_{ij}}$, the K_{ij2} coefficients are sines of the effective angles, and the K_{ij3} coefficients account for aerodynamic blockage as described above. The C_{ijl} ($l = 1, 2, 3, 4, 5, 6$) constants are positive or negative fractions of the projected prong spacing h for a given array geometry. To illustrate (6), consider its form for sensor 1 of array 1 (see figure 1*d*):

$$(U_{e_{11}})^2 = \left[\cos\alpha_{e_{11}}\left(U_0 - 0.8h\frac{\partial U}{\partial z} + 0.7h\frac{\partial U}{\partial y}\right) + \sin\alpha_{e_{11}}\left(V_0 - 0.8h\frac{\partial V}{\partial z} + 0.7h\frac{\partial V}{\partial y}\right)\right]^2 + k_{b_{11}}\left(W_0 - 0.8h\frac{\partial W}{\partial z} + 0.7h\frac{\partial W}{\partial y}\right)^2, \quad (7)$$

where $k_{b_{11}}$ is the blockage coefficient.

We solve these nine equations using an approach which clearly illustrates the character of the equations and the limitations of the probe. In this approach we obtain a function of V_i (velocity component V at an array centroid) and of the g_{ijk} (velocity component differences between values at the centroid of each array and values at the centres of the sensors of that array, where i is the array number, j the sensor number, and k the velocity component). By successively eliminating U_i and W_i for each array we obtain

$$F(V_i, g_{ijk}) = 0. \quad (8)$$

The g_{ijk} are the same for each array, consistent with the first-order gradient assumption. In the first step the difference velocities g_{ijk} are assumed to be zero and the Newton–Raphson method is applied to solve (8) for V_i at each of the three arrays separately. When this is done, the velocity components U_i and W_i can be obtained for each of the three arrays. Having now a first estimate of all components of velocities on all arrays, the difference velocities g_{ijk} can be computed and (8) can then be solved again with the updated values of the g_{ijk} for all three arrays. The process is repeated until the differences in the magnitudes of the updated values U_i, V_i, W_i for all three arrays and their previous estimates are smaller than a tolerance interval. The convergence is typically achieved after three iterations.

Equation (8) is a nonlinear algebraic function for which the imaginary roots can be ignored. There still remains, however, the problem of choosing between the remaining possible real roots. The shapes of the function $F(V_i)$ are shown by the lines in figure 4(*a*) for a determined set of g_{ijk} and for different values of the ratio V/U with W near zero. For the V/U ratio of -0.36, illustrated by the upper solid line, only one root occurs so it is obviously the physical solution. However, for a probe of this geometry and orientation with respect to the flow, as V/U increases the $F(V_i)$ curves are shifted downward. So for $V/U \approx 0$, illustrated by the lower solid line in the figure

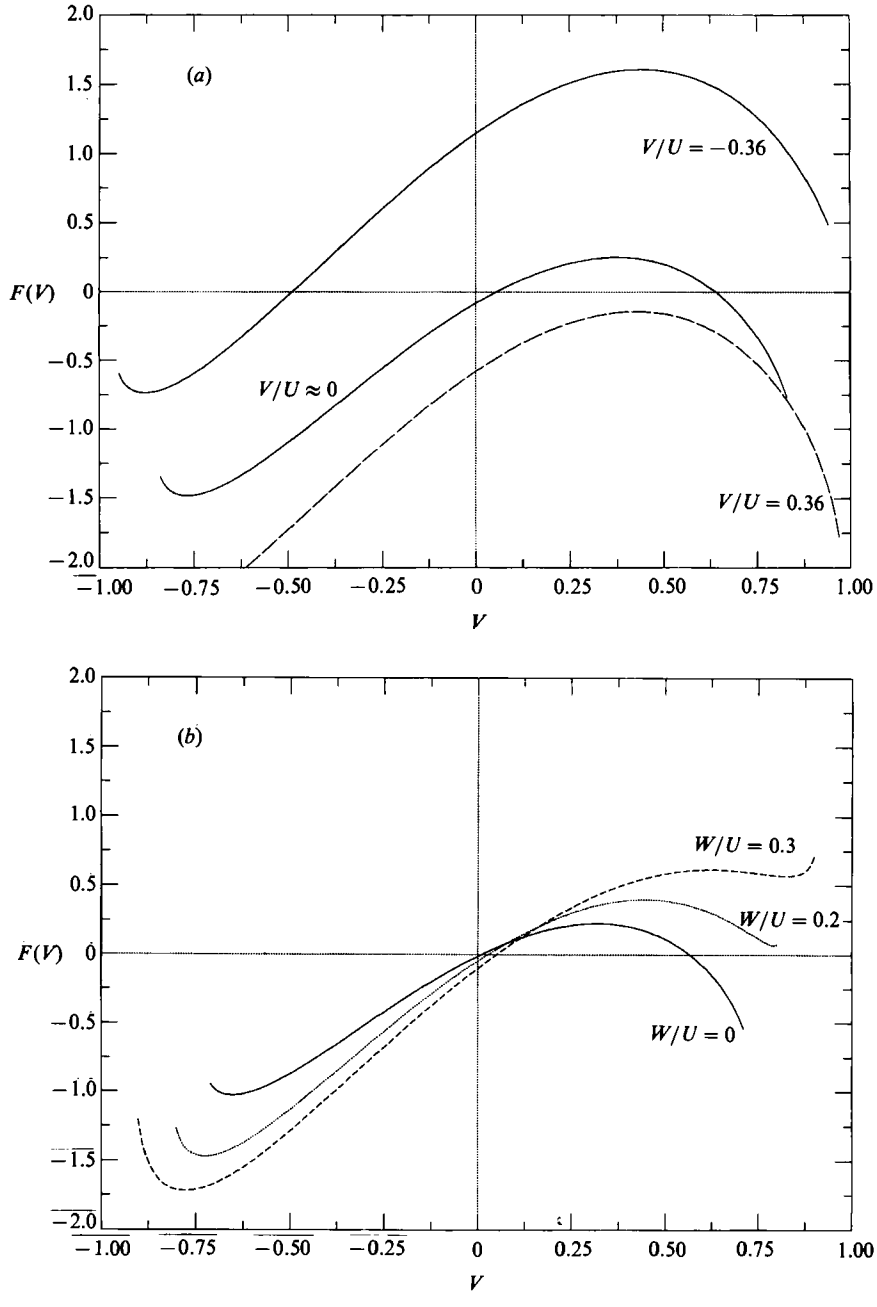

FIGURE 4. Function $F(V)$ curves, (*a*) for various V/U ratios and W nearly 0; (*b*) for various W/U ratios and V nearly 0.

for example, two real roots occur. One of these two solutions is always larger than a value corresponding to the maximum of the curve $F(V_i)$, which we will denote as $(V/U)_{cr}$. This critical value determines the range of uniqueness of the probe. It means that the probe can be used in a flow where the largest value of V/U occurring in the flow is expected to be smaller than the critical value, i.e. $(V/U)_L < (V/U)_{cr}$. In this case, although two real roots can be found, only the smaller one exists in the flow.

It is necessary to evaluate the factors determining $(V/U)_{cr}$ and then to construct the probe so as to make $(V/U)_{cr}$ as large as possible in order to have the range of uniqueness of the solution as large as possible. If W is increased, the curves $F(V_i)$ are lifted at the right-hand extremity, as seen in figure 4(*b*), making the problem of uniqueness less severe. Thus the $W = 0$ case is the most critical. For a probe with the geometrical arrangement of the wires shown in figure 1, the critical ratio can be expressed as

$$\left(\frac{V}{U}\right)_{cr} = \frac{\sin \alpha_{e_{i1}} \cos^2 \alpha_{e_{i2}}}{k_{b_{i2}} \cos \alpha_{e_{i1}}}. \tag{9}$$

In the ideal case where all the effective angles are the same and equal to 45° and there is no blockage effect, i.e. $k_{b_{i2}} = 1$, this value of $(V/U)_{cr}$ is 0.5. For the $\alpha_{e_{ij}}$ and $k_{b_{ij}}$ determined from calibration for the probe of figure 1, the average value of $(V/U)_{cr}$ for all three arrays is 0.36, corresponding to an angle of attack of the velocity vector to the probe of 19.8°.

Kreplin & Eckelmann (1979) have reported the angular deviation of the instantaneous velocity components from the mean flow direction in a turbulent channel flow. The probability density distribution of these deviations are available for distances from the wall ranging from about $y^+ = 3.5$–200. A maximum deviation of about $+16°$ and $-10°$ is reported for the positive and negative v-fluctuations at $y^+ = 10$, the probability density being asymmetric and displaying a positive skewness. From these estimates we can deduce values of $(V/U)_L \approx 0.3$ at $y^+ = 10$ and $(V/U)_L \approx 0.25$ at $y^+ = 40$. Thus, although the condition $(V/U)_L \leqslant (V/U)_{cr}$ is satisfied for the average of all three arrays of our probe, the values of $(V/U)_L$ become very close to $(V/U)_{cr} = 0.36$ as the wall is approached.

The fact that $(V/U)_L$ can be near $(V/U)_{cr}$ may also lead to an additional problem. Any error in measuring the E_{ij} voltage values moves the $F(V_i)$ curve up or down, thus changing its intersection with the abscissa and resulting in an error in the determination of V_i. It is obvious that the error will be highest near $(V/U)_{cr}$ (maximum of $F(V_i)$) because of the small slope in that region. It can also happen that the measurement error is large enough to cause the curve to fall under the abscissa and therefore to give no solution, even when the criterion $(V/U)_L \leqslant (V/U)_{cr}$ is satisfied. This situation is illustrated by the dashed line in figure 4(*a*) for $V/U = +0.36$. Although it is then known that the real solution is close to the critical one, i.e. $V/U \approx (V/U)_{cr}$, the dashed line in figure 4(*a*) shows that the method does not converge and no solution is found.

It is worthwhile to attempt to enlarge the range of uniqueness as much as possible. It can be increased by changing the geometrical arrangement of the sensors, but this is at the cost of making determination of the calibration coefficients much more complex. Taking that into account and having a relatively small number of cases where $V/U \approx (V/U)_{cr}$ (at $y^+ = 11.2$, 7.1 %, $y^+ = 18.3$, 2.5 % and $y^+ = 27.4$, 0.9 %), i.e. where the solution does not converge, we decided to keep the geometrical arrangement of figure 1 at present. We plan in the future to continue the development of the probe by altering this geometry and studying the effects.

The velocity at the centre of the probe is obtained from the velocities measured at each of the individual arrays and the cross-stream gradients determined at each time step. We can define, for example, the velocity component U_c (streamwise direction) for this probe as

$$U_c = U_3 + 1.2h\frac{\partial U}{\partial y} + 0.8h\frac{\partial U}{\partial z}. \tag{10}$$

Similar expressions are obtained for V_c and W_c by substituting for U with V and W, respectively, in (10).

5. Additional technical problems

5.1. *Streamwise velocity gradients*

The nine-sensor probe is not capable of directly measuring velocity gradients in the streamwise direction. In order to obtain these gradients, Taylor's hypothesis, which relates time derivatives to streamwise spatial derivatives by the relation $\partial/\partial x = -1/U_c\,\partial/\partial t$, must be used. Here U_c is a convection velocity which is often taken as the local mean velocity, but other choices have been used. The streamwise vorticity component can be determined directly from the measurements with this probe, but the normal and spanwise components involve the terms $\partial W/\partial x$ and $\partial V/\partial x$ which must be obtained from Taylor's hypothesis. Piomelli, Balint & Wallace (1989) have compared the r.m.s. values of

$$T_{1j} = \frac{\partial U_j}{\partial t}; \quad T_{2j} = \bar{U}_1 \frac{\partial U_j}{\partial x_1}; \quad T_{3j} = \frac{\partial}{\partial x_k}(U_j U_k) \tag{11}$$

and the correlation coefficient between T_{1j} and T_{2j} for a large-eddy simulation (LES) of a turbulent channel flow in order to evaluate the magnitude and phase relationships of the terms in Taylor's hypothesis. They find negligible differences everywhere above the buffer layer between the r.m.s. values of the terms in (11) and a 0.95 or greater correlation coefficient between T_{1j} and T_{2j}. Somewhat larger differences do appear in the range $y^+ = 15$–30, but these differences are not very substantial even there. This LES evaluation gives strong support to Taylor's hypothesis. Comparing r.m.s. values of $\partial u_1/\partial x_k$, $(k = 1, 2, 3)$ and of $\partial u_j/\partial x_1$, $(j = 1, 2, 3)$ from this LES with values from the direct simulation of Kim *et al.* (1987) and with measurements with an earlier version of our nine-sensor probe, Piomelli *et al.* (1989) show that the LES is sufficiently reliable to evaluate Taylor's hypothesis in and above the buffer layer even though the subgrid scales, which in the study cited accounted for less than 8% of the total Reynolds stress, must be modelled. Thus, the use of Taylor's hypothesis for the boundary-layer measurements reported in Part 2 appears quite justified.

5.2. *Voltage corrections due to ambient temperature variation*

The anemometer bridge circuit output is sensitive to variations in the ambient temperature of the open-return wind tunnel used in this work; this is an important effect, especially when the bridge is operated at the low overheat ratio necessary to minimize thermal interference (1.22 in the experiment reported herein). For a small temperature variation (2–3 °C) the bridge output voltage is nearly linear with temperature, as seen in figure 5 for sensor 1 of array 1. The temperatures were measured over an 11 h interval and varied from 26.9–29.0 °C. Thus the effect of temperature variation can be easily corrected for each value of the digitized voltages if the ambient temperature is also sampled. In the experiment reported in Part 2 the temperature ranged between 27.2–28.0 °C when turbulence data were recorded. These temperatures were continuously monitored with a digital thermistor thermometer. Tests run on several calibration data files showed that the K_{ijk} calibration coefficients of (6) were virtually independent of the reference temperature to which the measured voltages were corrected.

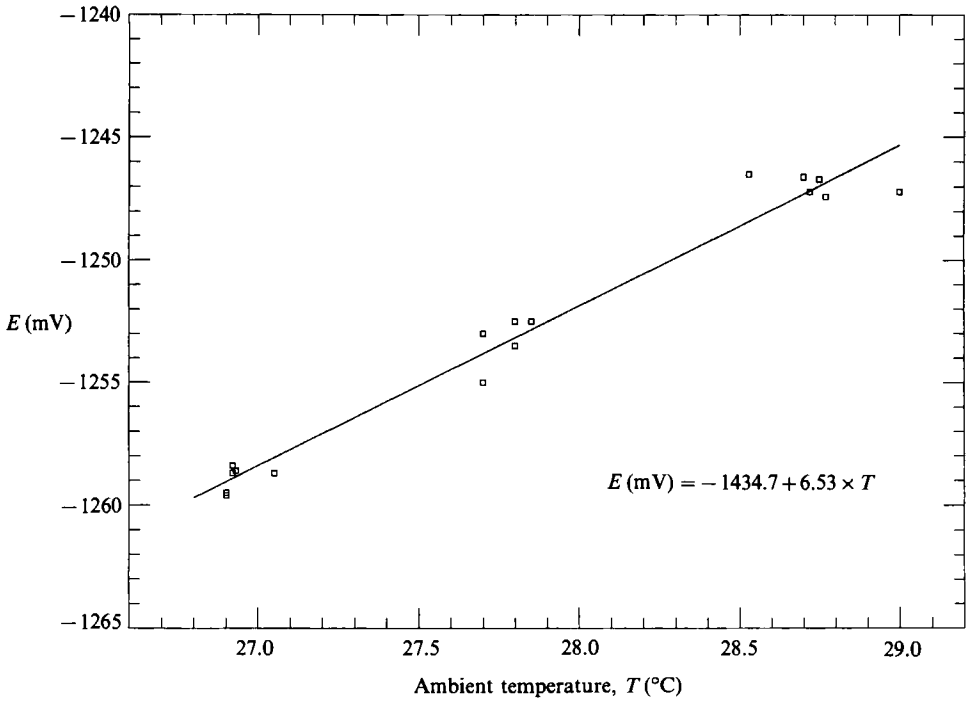

FIGURE 5. Variation of the anemometer bridge voltage with temperature for sensor (1, 1) during calibration and data acquisition.

5.3. *Cross-talk effects through common prongs*

We chose to use a common prong for the three sensors of each array to reduce the aerodynamic disturbance from the presence of the probe. Of course this can introduce electrical cross-talk between the anemometer circuits. Previous experience showed that the common-prong resistances should be about 0.1 Ω to avoid anemometer bridge circuit instabilities and significant cross-talk in the measured voltages for the overheat ratio of 1.22 used in this study. In an earlier version of the probe, the common-prong resistances were lowered by nickel plating them more than the surrounding prongs. The requirement was that the plating should be thick enough to bring the resistance down but still leave a prong thickness that will not substantially increase the aerodynamical blockage. To reduce the plating thickness for the probe used in this investigation each common tungsten prong was first plated with copper. This significantly decreased the resistance to about 0.08 Ω with a much smaller increase in prong diameter compared to nickel plating. Then the tips of the prongs were plated with a thin layer of nickel in order to facilitate welding of the tungsten sensors. This procedure eliminated the circuit instabilities and also decreased the common prong thickness.

To check for any evidence of electrical cross-talk through the common ground connection, a rather simple test was made as illustrated in figure 6. A variable common ground resistance between two independent single-sensor probes was introduced. In order to simulate the nine-sensor probe case, the single-sensor probes used in the test had 2.5 μm diameter tungsten sensors. The common resistance was adjusted to 0.08 Ω (which is the actual value of the nine-sensor component prongs resistances). The anemometer bridges were then balanced independently at an overheat ratio of 1.22. Probe 1 was positioned in the wind tunnel free-stream core

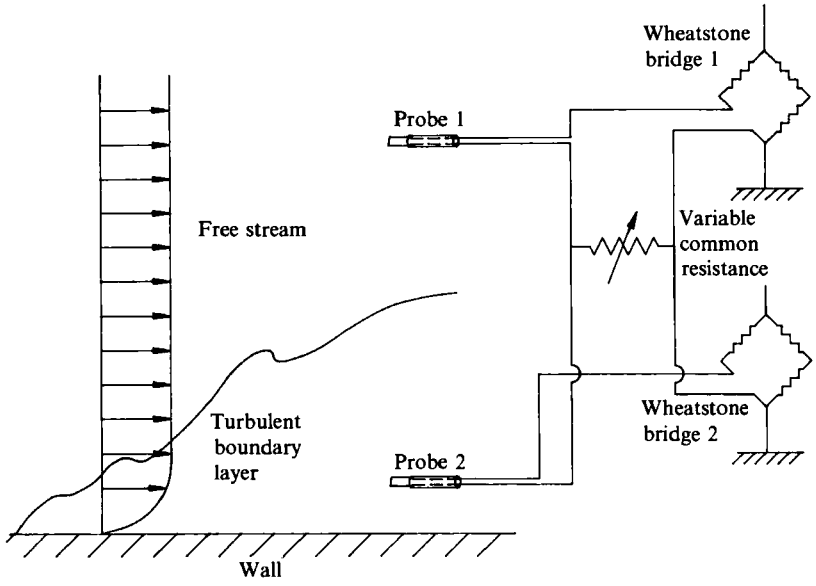

FIGURE 6. Procedure for testing for electrical cross-talk through a variable common resistance.

and probe 2 was lowered into the turbulent boundary-layer wall region. Output signals of the probes were monitored on storage oscilloscopes, first with one probe off while operating the other and then with both probes operating simultaneously. No instabilities occurred in circuits 1 or 2 while in simultaneous operation and no fluctuations appeared on the signal from probe 1 in the free-stream flow. It was apparent that the fluctuations sensed by probe 2 do not significantly contaminate circuit 1 through the common prong. The common-prong resistance was then increased in 0.01 Ω steps. No contamination of the free-stream flow signal was seen up to a value of 0.13 Ω; at that common-prong resistance value the circuits became unstable when operated together.

5.4. *Aerodynamical blockage effects and thermal contamination*

In the case of a horizontal single-sensor probe, the blockage effect is due to the flow through the prongs being accelerated as the pitch angle increases, thereby changing the wire cooling at higher pitch angles of attack than would have occurred if the prongs were not present, as illustrated in figure 7 (*a*). For the same prong spacing, the thicker the prongs the stronger will be the blockage effect. In order to reduce the blockage effects, the prong diameters cannot be reduced too much because very thin prong tips will mechanically vibrate as well as begin to act as sensors themselves. The latter problem has adverse effects on blockage reduction as well as undermining the assumptions on which the sensor response was determined. Therefore one should determine a prong thickness and spacing that will minimize this effect.

Owing to the complex geometrical configuration of the nine-sensor probe, thermal contamination and aerodynamical blockage effects are very difficult to separate. Instead, we decided to break up the problem into basic geometrical configurations, each of which was simulated by a pair of prongs and a single sensor. For a 2.5 μm sensor diameter, prong spacings of 0.5 and 1 mm and prong tip thicknesses of 0.05 mm and 0.1 mm were tried with two test probes. The probes were pitched and yawed at free-stream velocities ranging from about 1.5 to 3.5 m/s. Blockage

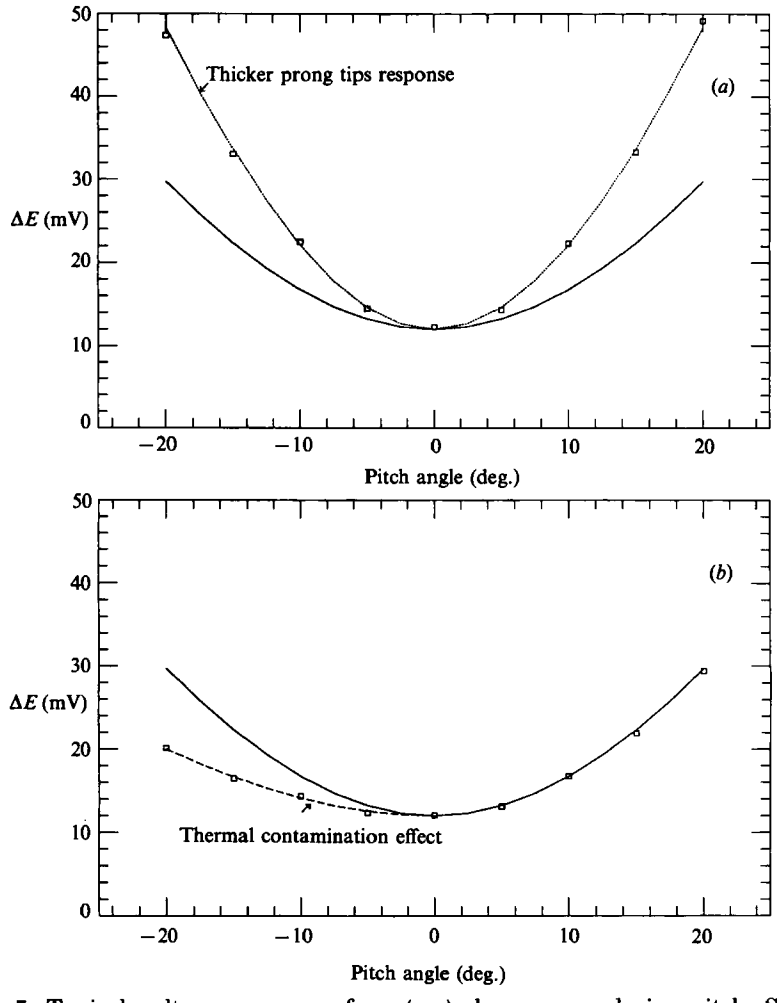

FIGURE 7. Typical voltage response of an (x, z)-plane sensor during pitch. Solid lines: ideal response of a sensor (with blockage equal to unity and effective angle of 45°); (*a*) □, measured response for a probe with thick prongs and high blockage coefficients; (*b*) □, measured asymmetric response due to thermal interference within an array of the nine-sensor probe.

coefficients and cooling response curves indicated that a prong spacing of about 0.5–0.6 mm and a tip thickness of about 0.05–0.08 mm gave an average blockage coefficient of about 1.15 for the single sensor probes. One should anticipate higher blockage values for multi-prong configurations with the same spacing and thickness (k_b of about 1.3 to 2.0). However, even these k_b values prevent non-uniqueness or non-convergence problems. Furthermore, with these prong thicknesses and spacings, the data did not indicate that the prong tips were acting as sensors at the higher pitch angles of 15°–20°.

The thermal contamination was checked by comparing the pitch/yaw response curves when the nine-sensor probe was tested with all three arrays operating to the curves obtained with only one or with two arrays operating. This showed no evidence of thermal contamination from array to array. However, there is thermal contamination within an individual three-sensor array, even at the low overheat used here; the effect is to distort the symmetry of pitch response for sensors in the

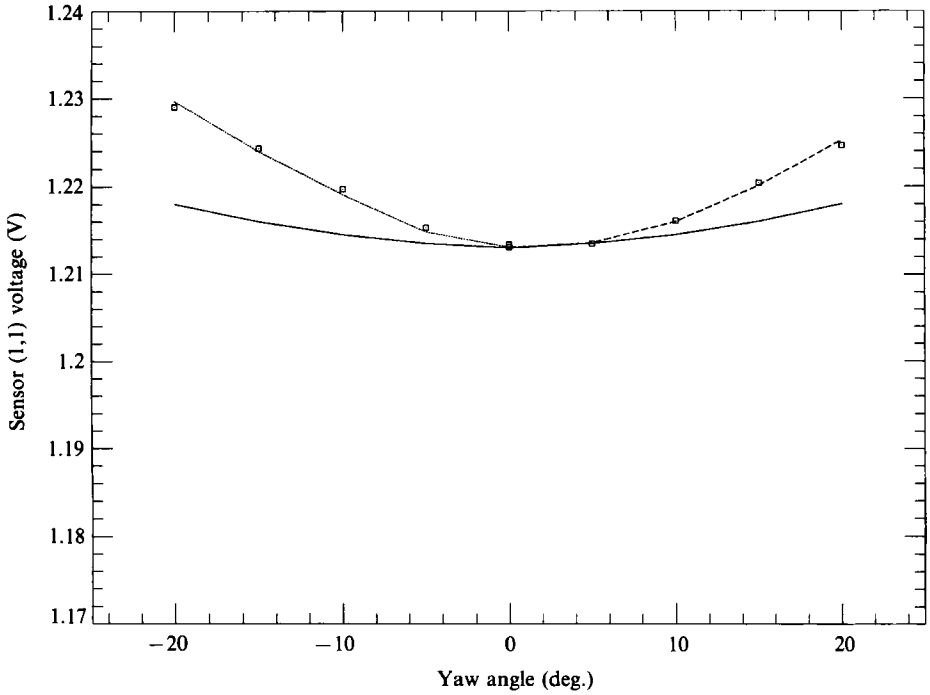

FIGURE 8. Voltage response of sensor (1, 1) during yaw. Solid line, ideal response of a sensor (with blockage equal to unity and effective angle of 45°); dotted line, calibration fit for negative yaw; dashed line, calibration fit for positive yaw.

(x, z)-plane of figure 1(*d*) (or of yaw response of sensors in the (x, y)-plane) as illustrated in figure 7(*b*).

The thermal contamination acts like an effective aerodynamical blockage acting on either the negative or the positive pitch response of an (x, z)-plane sensor or on the yaw response of an (x, y)-plane sensor. In fact, both aerodynamical and thermal effects can be lumped into apparent 'positive' or 'negative' blockage coefficients with values due to asymmetry of 2.0 or more (here 'positive' or 'negative' refer to the sign of the pitch/yaw angle and not to the sign of the blockage coefficient).

6. Probe calibration method

The probe was placed in the nominally irrotational free-stream core of the wind tunnel and the calibration coefficients were obtained by pitching and yawing the probe for mean speeds corresponding to y^+ measurement locations in the boundary layer as illustrated by the yaw calibration response of sensor (1, 1) in figure 8. It was also aligned with the mean flow and the mean speed varied over a range expected for the boundary layer as illustrated for sensor (1, 1) in figure 9. The calibration coefficient set is thus determined for flow conditions that mimic the turbulent flow conditions as closely as possible. These coefficients are found by least-square fits of calibration measurements over the range of variation of U, V and W (i.e. U_∞, ϕ, and θ, where U_∞ is the free-stream velocity and ϕ and θ are the pitch and yaw angles) expected in the turbulent flow. A total of 36 coefficients result from those fits.

The ideal curves E_{1i} versus yaw angle θ, for sensor 1 of array i, *or* E_{ij} versus pitch angle ϕ for sensor ($j = 2, 3$) of array i should be symmetrical because they are expected to approximately follow 'cosine law' cooling. The experimental curves

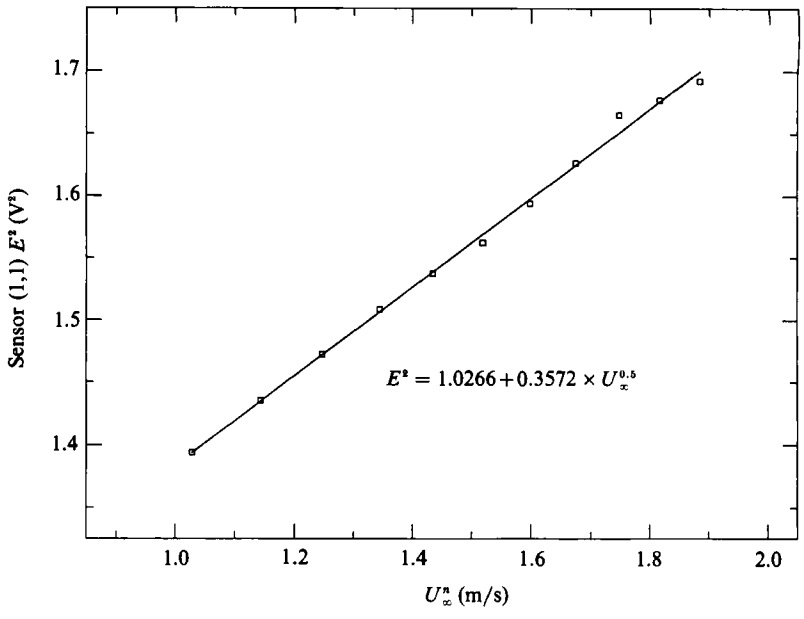

FIGURE 9. Linear fit of sensor (1, 1) E^2 *vs.* U_∞^n response during free-stream velocity variation.

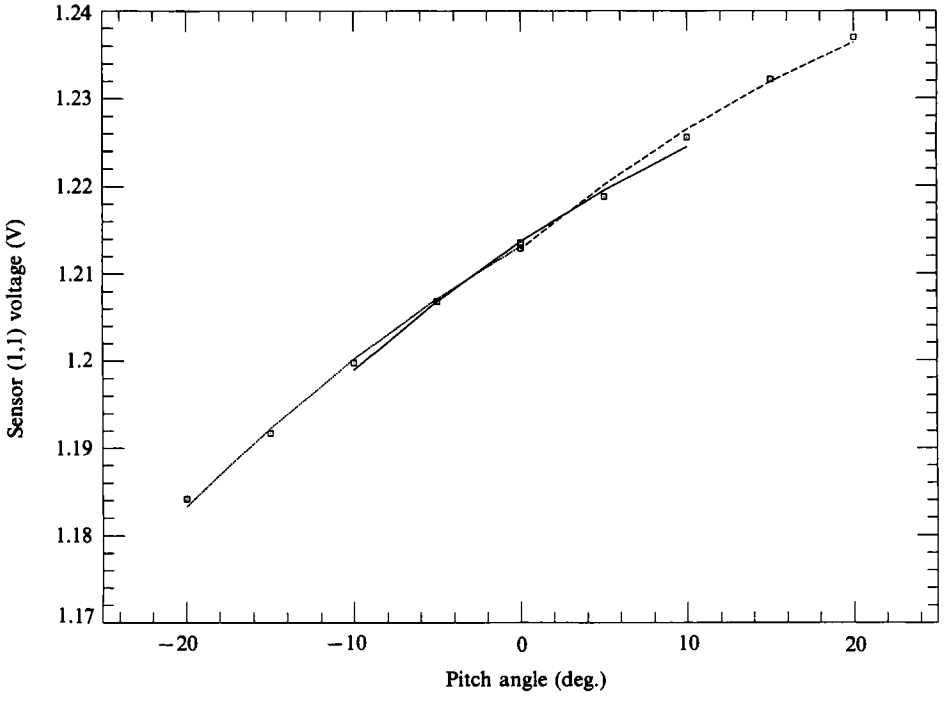

FIGURE 10. Voltage response of sensor (1, 1) during pitch. Solid line, calibration fit for middle-range pitch; dotted line, calibration fit for negative pitch; dashed line, calibration fit for positive pitch.

show a slight asymmetry, as mentioned above, and suggest that the 'blockage' effect is not always the same when the velocity vector attacks the probe axis at a positive or negative angle in yaw or pitch. For example, the voltage response of sensor (1, 1) during yaw in figure 8 shows this slight asymmetry (the solid line in the figure is the

response of an ideal sensor with an effective angle $\alpha_e = 45°$ and a blockage coefficient $k_{b_{11}} = 1.0$). This observation suggested the possibility of defining positive angle blockage coefficients $k^+_{b_{ij}}$ and negative angle blockage coefficients $k^-_{b_{ij}}$ for positive or negative values of pitch/yaw angles greater than or equal to 10° as mentioned before in §5.4. For sensor (1, 1), $k^+_{b_{11}} = 2.38$ and $k^-_{b_{11}} = 2.35$.

Drawing on our experience with the 'positive' and 'negative' blockage coefficients, we extended this approach to other coefficients, e.g. the King's law slopes and effective angles. The least-square fits of calibration data were divided into three calibration ranges: high negative pitch/yaw angles, near zero pitch/yaw angles and high positive pitch/yaw angles, as seen in figure 10 for pitch. For the data in figure 10, the effective angles in these three ranges are 36.0°, 39.9° and 46.1° respectively. In effect, this means that the influence of the effective cooling velocity on these coefficients is taken into account as suggested by Bruun & Tropea (1980). The drawback to using positive and negative values of the calibration coefficients is, of course, that the data analysis program now must chose between three sets of calibration coefficients each time it solves (8).

7. Testing the accuracy of the probe

7.1. *Tests*

Test programs evaluate the errors in velocity components as well as the spurious gradients and spurious vorticity components measured by the probe during the calibration in irrotational flow. Figures 11(*a*) and 11(*b*) show, as solid lines, the velocity components *induced* during calibration by variation of the tunnel's speed and pitch and yaw angles respectively. The data points shown are those obtained using the *measured* calibration voltages and the calibration coefficients found as described in §6. For this particular set of test data, a slight probe misalignment of $+1.5°$ in pitch and $-2°$ in yaw is seen in figures 11(*a*) and 11(*b*) where V and W are not exactly zero for the tunnel speed variation or at zero pitch and yaw respectively. Additional terms were incorporated in the cooling equations in order to account for these alignment errors. These corrections, however, are valid only for small angular misalignments (less than 3°). The measured velocities match the induced velocities very well for all speeds and angles of attack except at the quite high pitch angle of $+20°$. Figure 12 shows the spurious values of the vorticity components which result from these errors in the measurement of the induced velocity components in the free-stream irrotational flow where the vorticity vector should be zero. Thus, it is obvious that small velocity errors can be amplified into not insignificant spurious vorticity errors. These values are a good indicator of the entire measurement system noise.

Figure 13(*a–c*) shows the probability density distributions of the spurious vorticity components measured in the free-stream core of the wind tunnel after the turbulent boundary-layer experiment described in Part 2. The widths of these distributions are another measure of the noise of the entire measuring system. The two cross-stream components ω_y and ω_z have no spurious values larger than about $30\ s^{-1}$. The streamwise component ω_x has rare occurrences of spurious values of about $90\ s^{-1}$. These values give a high signal-to-noise ratio when compared to peak values of $\pm 1200\ s^{-1}$ near the wall in the boundary layer. The fact that the noise in the ω_x signal is larger than that in the ω_y and ω_z signals may be due to the necessary use of Taylor's hypothesis in the latter. These distributions are qualitatively consistent with the relative magnitudes of the spurious vorticity components found in the calibration data of figure 12. The probability density distributions of the

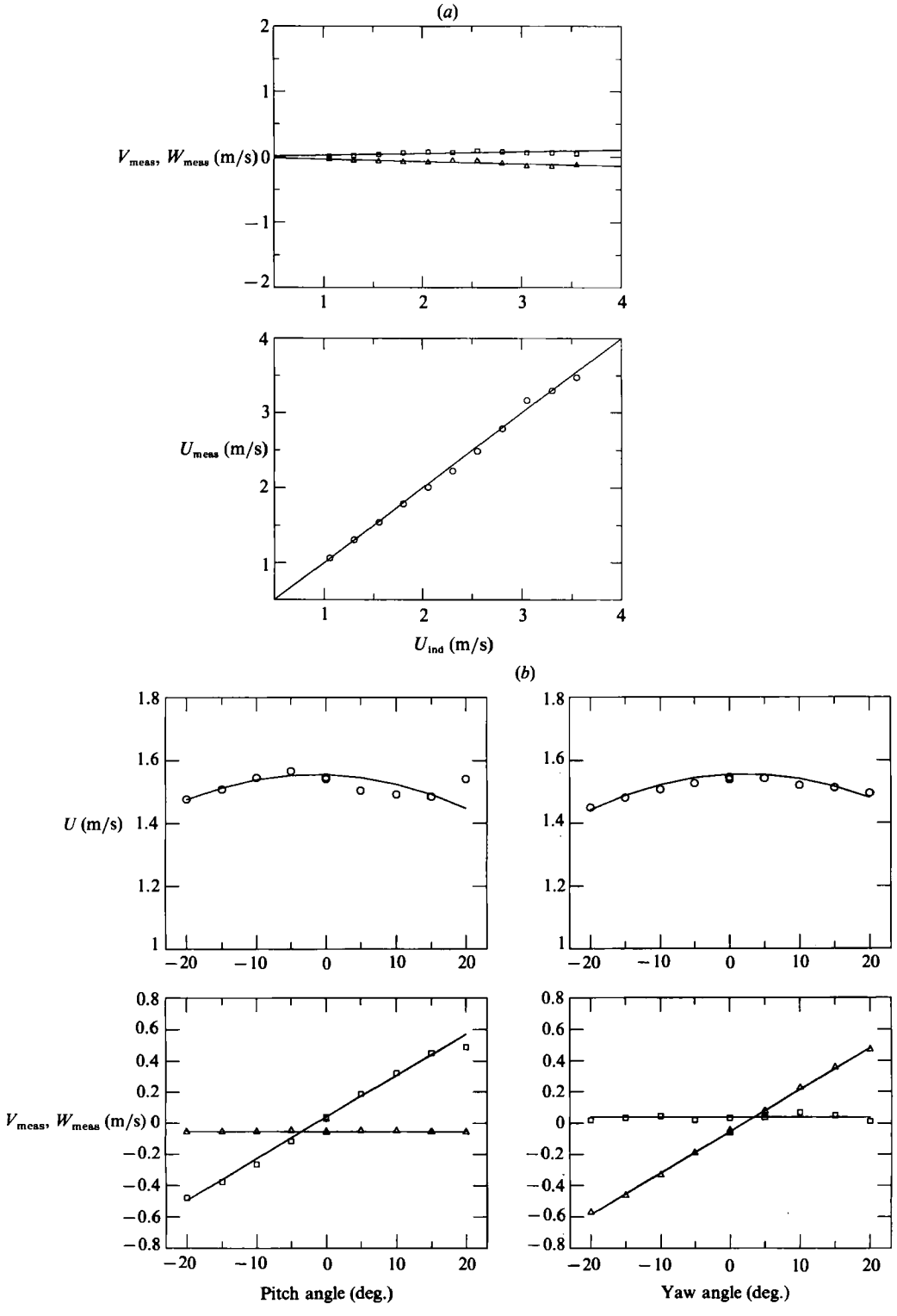

FIGURE 11. Induced and measured velocity components during (*a*) tunnel speed variation, and (*b*) pitch and yaw variations at constant speed. Solid lines, induced values; ○; measured streamwise component U, □, measured normal component V, △, measured spanwise component W.

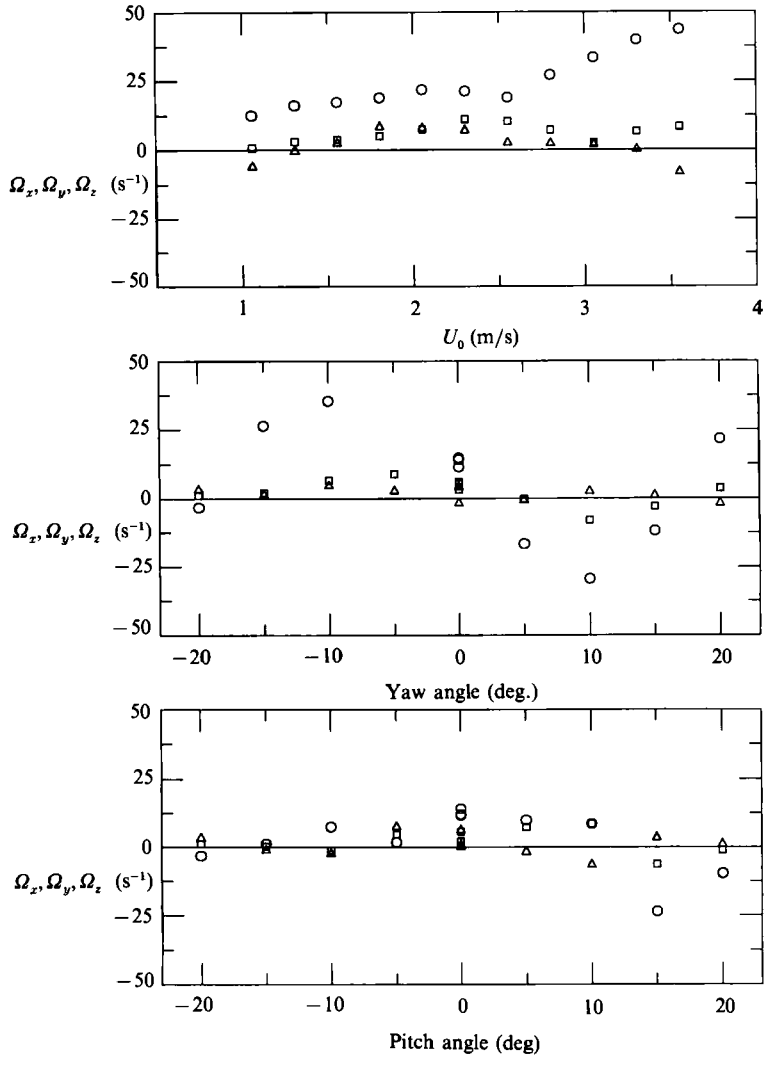

FIGURE 12. Spurious vorticity components sensed in the free stream during the calibration: ○, streamwise component Ω_x, □, normal component Ω_y; △, spanwise component Ω_z.

spurious vorticity components shown in figure 13(*a–c*) will be compared in Part 2 to the distributions measured in the boundary layer for the turbulent vorticity components.

Figure 14 compares the distribution of the mean velocity gradient $\partial\bar{U}/\partial y$ (of the turbulent boundary layer described in Part 2) measured *directly* with the nine-sensor probe (the instantaneous $\partial U/\partial y$ values are averaged for the data set at each y^+ position) with the derivative of a fit of published mean velocity measurements given by Spalding (1961). Also shown as a solid line is the derivative of the logarithmic law for $y^+ > 30$ with constants given by Coles (1962). As mentioned earlier, it has been shown by Böttcher & Eckelmann (1985) that it is very difficult to obtain accurately the mean velocity gradient from the average of velocity differences when they are directly measured over small distances of only a few Kolmogorov microscales. Therefore, this is a good test of the capability of the nine-sensor probe to resolve instantaneous velocity gradients accurately. The comparison in figure 14 shows just

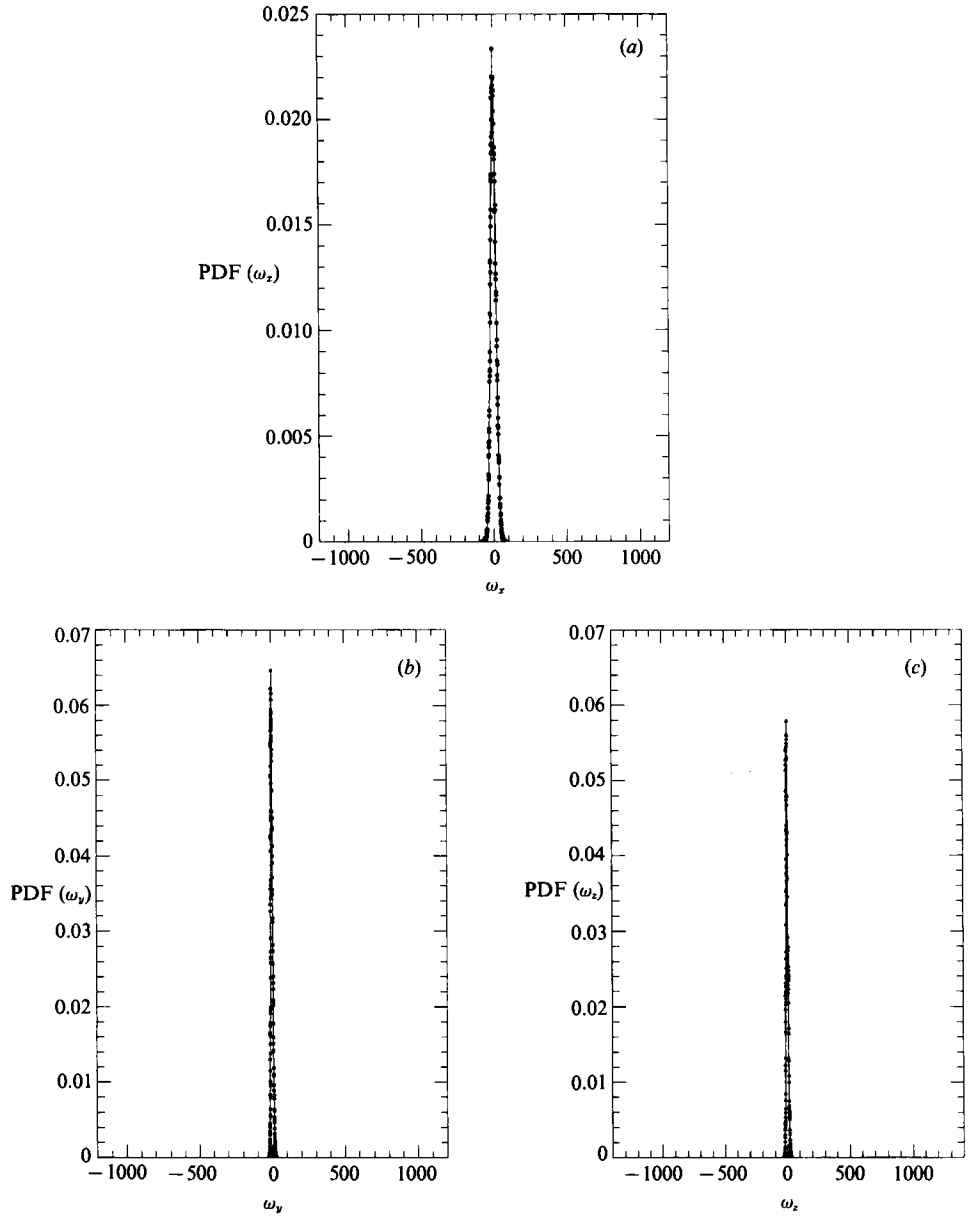

FIGURE 13. Probability density functions of fluctuating vorticity components measured in the irrotational free stream. (*a*) $P(\omega_x)$, (*b*) $P(\omega_y)$, (*c*) $P(\omega_z)$.

how well the probe can directly measure this mean gradient. For $y^+ < 50$ the directly measured gradients are within 10% or less of the derivatives of the curve fits of the mean velocity. This relative error increases, of course, as the absolute magnitude decreases with increasing distance from the wall.

7.2. *Error estimates*

The free-stream velocity in the tunnel was measured with a Pitot tube connected to a Barocel electronic monometer. The pressure was determined with an accuracy of 10^{-4} Torr thus giving an accuracy of 1% for U_∞ in the 1.0–3.5 m/s speed range. The

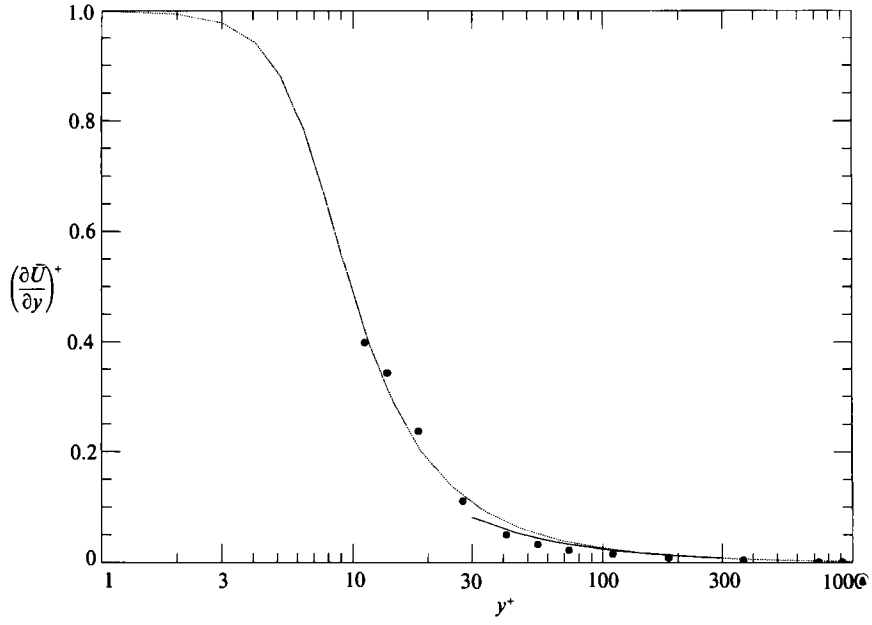

FIGURE 14. Distribution of the mean velocity gradient $\partial \bar{U}/\partial y$ across the boundary layer. Dotted line, Spalding (1961); solid line, Coles (1962); ●, values directly measured by the nine-sensor probe.

accuracy of the velocity and vorticity fluctuation measurements were estimated by applying the Newton–Raphson algorithm to the free-stream velocity variation and pitch/yaw calibration data, as mentioned previously. During the free-stream calibration (figure 11*a*) the error for the streamwise component U in the 1.0–3.5 m/s speed range was from 0.005–0.035 m/s. For the pitch/yaw calibration (figure 11*b*), at 1.55 m/s, the average absolute errors for velocity components U, V, and W were 0.015, 0.016, 0.006 m/s, respectively, over the $\pm 15°$ range. The average spurious vorticity component values resulting from these velocity errors (figure 12) occurring in the calibration in the free-stream core were $\bar{\Omega}_x = 17.1\ \mathrm{s}^{-1}$, $\bar{\Omega}_y = 7.1\ \mathrm{s}^{-1}$, $\bar{\Omega}_z = 7.9\ \mathrm{s}^{-1}$, respectively. These average spurious values correspond respectively to 12.0%, 4.6%, 4.4% of the average of the r.m.s. vorticity fluctuations ω_x, ω_y, ω_z measured over the $y^+ = 13$–50 region of the boundary layer as described in Part 2. When the free-stream core was directly sampled as one of the points in the boundary-layer experiment (figure 13*a–c*), the measured average spurious vorticity values were $\bar{\Omega}_x = 18.5\ \mathrm{s}^{-1}$, $\bar{\Omega}_y = 6.6\ \mathrm{s}^{-1}$, and $\bar{\Omega}_z = 8.1\ \mathrm{s}^{-1}$, corroborating the result obtained from calibration.

8. Conclusions

This paper (Part 1) describes a small nine-sensor hot-wire probe capable of simultaneously measuring the velocity and vorticity vectors in turbulent flow. Moreover, for the first time the velocity vector is measured while accounting for the variation of the velocity field across the sensing area of the probe. The distance over which velocity gradients are determined is about 6.3 Kolmogorov microscales or 10.9 viscous lengths when positioned at $y^+ = 11.2$ in a thick boundary layer at $R_\theta = 2685$. For a test case, where a set of velocity components similar to those occurring in the

boundary layer are induced in a uniform irrotational flow similar to that occurring in the boundary layer, each of the three arrays of the probe are able to determine U, V, and W within an average absolute error of 0.016 m/s or less. These errors result in average vorticity component errors of 12.0%, 4.6% and 4.4% of the average of the r.m.s. vorticity fluctuations ω_x, ω_y, and ω_z respectively in the $y^+ = 13$–50 region of the boundary layer. The probe is capable of directly measuring the mean velocity gradient of the turbulent boundary layer (a stringent test) with very good accuracy. Therefore this nine-sensor probe appears to be suitable for measurements of the statistical properties of the boundary-layer vorticity field with acceptable resolution and accuracy. These measurements of the turbulent vorticity fluctuations will be reported in Part 2 of this paper.

The authors are most grateful for the steadfast support of the National Science Foundation and its Fluid Dynamics Program Managers, George Lea, Dick Miksad and Stephen Traugott, over the duration of this research. It was not always evident that the probe could be made to work, so their faith in us is especially appreciated. Most recently the project has been funded by NSF Grant No. MSM-8610369 supplemented by DOE Grant No. DE-FG05-88ER13838. We are also grateful to numerous colleagues for helpful discussions, most especially to Peter Bernard, Ron Blackwelder, Bob Brodkey, Helmut Eckelmann, Barsam Marasali and Ugo Piomelli.

REFERENCES

ANTONIA, R. A., BROWNE, L. W. B. & SHAH, D. A. 1988 Characteristics of vorticity fluctuations in a turbulent wake. *J. Fluid Mech.* **189**, 349–365.

BALINT, J.-L., VUKOSLAVČEVIĆ, P. & WALLACE, J. M. 1987 A study of the vortical structure of the turbulent boundary layer. In *Advances in Turbulence* (ed. G. Comte-Bellot & J. Mathieu), pp. 456–464. Springer.

BALINT, J.-L., WALLACE, J. M. & VUKOSLAVČEVIĆ, P. 1991 The velocity and vorticity vector fields of a turbulent boundary layer. Part 2. Statistical properties. *J. Fluid Mech.* **228**, 53–86.

BÖTCHER, J. & ECKELMANN, H. 1985 Measurement of the velocity gradient with hot-film probes. *Exps Fluids* **3**, 87–91.

BRADSHAW, P. 1975 *An Introduction to Turbulence and its Measurement*, 2nd edn, pp. 121–126. Pergamon.

BRUUN, H. H. & TROPEA, C. 1980 Calibration of normal, inclined and x-array hot-wire probes. *Sonderforschungbereich*, vol. 80. University of Karlsruhe.

CHAMPAGNE, F. H., SLEICHER, C. A. & WEHRMANN, O. H. 1967 Turbulence measurement, with inclined hot-wires. Part 1. Heat transfer experiments with inclined hot-wires. *J. Fluid Mech.* **28**, 153–176.

COLES, D. E. 1962 The turbulent boundary layer in compressible fluid. Appendix A: a manual of experimental practice for low speed flow. *Rand Rep.* R403R-PR, ARC24473.

CORRSIN, S. & KISTLER, A. L. 1954 The free-stream boundaries of turbulent flows. *NACA TN* 3133.

ECKELMANN, H., NYCHAS, S. G., BRODKEY, R. S. & WALLACE, J. M. 1977 Vorticity and turbulence production in pattern recognized turbulent flow structures. *Phys. Fluids* **20**, S225–S231.

FALCO, R. E. 1983 New results, a review and synthesis of the mechanism of turbulence production in boundary layers and its modification. *AIAA*-83-0377.

FOSS, J. F. 1981 Advanced techniques for transverse vorticity measurements. In *Proc. 7th Biennial Symp. on Turbulence, University of Missouri-Rolla*, pp. 208–218.

FOSS, J. F., ALI, S. K. & HAW, R. C. 1987 A critical analysis of transverse vorticity measurements in a large plane shear layer. In *Advances in Turbulence* (ed. G. Comte-Bellot & J. Mathieu), pp. 446–455. Springer.

FOSS, J. F., KLEWICKI, C. L. & DISIMILE, P. J. 1986 Transverse vorticity measurements using an array of four hot-wires. *NASA CR* 178098.

FOSS, J. F. & WALLACE, J. M. 1989 The measurement of vorticity in transitional and fully developed turbulent flows. In *Advances in Fluid Mechanics Measurements* (ed. M. Gad-el-Hak). Lecture Notes in Engineering, vol. 45, pp. 263–321. Springer.

HAW, R. C., FOSS, J. K. & FOSS, J. F. 1989 The vortical properties of the high speed region in a plane shear layer and its parent boundary layer. In *Advances in Turbulence*, vol. 2 (ed. H.-H. Fernholz & H. E. Fiedler), pp. 90–95. Springer.

KASTRINAKIS, E. G. 1976 An experimental investigation of the fluctuations of the streamwise components of the velocity and vorticity vectors in a fully developed turbulent channel flow. Dissertation, Georg-August Universität zu Göttingen.

KASTRINAKIS, E. G., ECKELMANN, H. & WILLMARTH, W. W. 1979 Influence of the flow velocity on a Kovasznay type vorticity probe. *Rev. Sci. Instrum.* **50**, 759–767.

KASTRINAKIS, E. G. & ECKELMANN, H. 1983 Measurement of streamwise vorticity fluctuations in a turbulent channel flow. *J. Fluid Mech.* **137**, 165–186.

KASTRINAKIS, E. G., NYCHAS, S. G. & ECKELMANN, H. 1983 Some streamwise vorticity characteristics of coherent structures. In *Structure of Complex Turbulent Shear Flow* (ed. R. Dumas & L. Fulachier), pp. 31–40. Springer.

KASTRINAKIS, E. G., WALLACE, J. M., WILLMARTH, W. W., GHORASHI, B. & BRODKEY, R. S. 1977 On the mechanism of bounded turbulent shear flows. In *Structure and Mechanisms of Turbulence I.* Lecture Notes in Physics, vol. 75, pp. 175–189.

KIM, J., MOIN, P. & MOSER, R. 1987 Turbulence statistics in fully developed channel flow at low Reynolds number. *J. Fluid Mech.* **177**, 133–166.

KIM, J.-H. & FIEDLER, H. 1989 Vorticity measurements in a turbulent mixing layer. In *Advances in Turbulence*, vol. 2 (ed. H.-H. Fernholz & H. E. Fiedler), pp. 267–271. Springer.

KING, L. V. 1914 On the convection of heat from small cylinders in a stream of fluid. *Phys. Trans. R. Soc. Lond.* A **214**, 373–432.

KISTLER, A. L. 1952 The vorticity meter. M.S. Thesis, The Johns Hopkins University.

KLEBANOFF, P. S. 1954 Characteristics of turbulence in a boundary layer with zero pressure gradient. *NACA TN* 3178.

KLEWICKI, J. C. & FALCO, R. E. 1990 On accurately measuring statistics associated with small scale structure in turbulent boundary layers using hot-wire probes. *J. Fluid Mech.* **219**, 119–143.

KOVASZNAY, L. S. G. 1950 *Q. Prog. Rep. Aero. Dept. Contract* NORD-8036-JHB-39. The Johns Hopkins University.

KOVASZNAY, L. S. G. 1954 Turbulence measurements. In *Physical Measurements in Gas Dynamics and Combustion*, vol. 10 (ed. R. W. Landenbuerg, B. Lewis, R. N. Pease & H. S. Taylor), pp. 213. Princeton University Press.

KREPLIN, H.-P. & ECKELMANN, H. 1979 Instantaneous direction of the velocity vector in a fully developed turbulent channel flow. *Phys. Fluids* **22**, 1210–1211.

LANG, D. B. 1985 Laser Doppler velocity and vorticity measurements in turbulent shear layers. Ph.D. Dissertation, California Institute of Technology.

LAUFER, J. 1953 The structure of turbulence in fully developed pipe flow. *NACA TN* 2954.

METCALFE, R. W., ORSZAG, S. A., BRACHET, M. E., MENON, S. & RILEY, J. J. 1987 Secondary instability of a temporally growing mixing layer. *J. Fluid Mech.* **184**, 207–243.

NYCHAS, S. G., KASTRINAKIS, E. G. & ECKELMANN, H. 1985 On certain aspects of vorticity dynamics and turbulent energy production. *Lecture Notes in Physics*, vol. 235, pp. 269–278.

PAO, Y. H. 1965 Structure of turbulent velocity and scalar fields at large wave numbers. *Phys. Fluids* **8**, 1063–1075.

PIOMELLI, U., BALINT, J.-L. & WALLACE, J. M. 1989 On the validity of Taylor's hypothesis for wall-bounded turbulent flows. *Phys. Fluids* A **1**, 609–611.

ROGERS, M. M. & MOIN, P. 1987 The structure of the vorticity field in homogeneous turbulent flows. *J. Fluid Mech.* **176**, 33–66.

SPALART, P. R. 1988 Direct simulation of a turbulent boundary layer up to $R_\theta = 1410$. *J. Fluid Mech.* **187**, 61–98.

SPALDING, D. B. 1961 A single formula for the law of the wall. *Trans. ASME* E: *J. Appl. Mech.* **28**, 455–457.

TENNEKES, H. & LUMLEY, J. L. 1972 *A First Course in Turbulence.* MIT Press.

TOWNSEND, A. A. 1951 The structure of the turbulent boundary layer. *Proc. Camb. Phil. Soc.* **47**, 375–395.

VUKOSLAVČEVIĆ, P. & WALLACE, J. M. 1981 Influence of velocity gradients on measurements of velocity and streamwise vorticity with hot-wire X-array probes. *Rev. Sci. Instrum.* **52**, 869–879.

VUKOSLAVČEVIĆ, P., WALLACE, J. M. & BALINT, J.-L. 1990 The simultaneous measurement of the velocity and vorticity vectors in turbulent flow using hot-wire anemometry. *Rep.* TRL-90-1. University of Maryland, Dept. of Mech. Engng.

WALLACE, J. M. 1986 Methods of measuring vorticity in turbulent flows. *Exps Fluids* **4**, 61–71.

WALLACE, J. M., BRODKEY, R. S. & ECKELMANN, H. 1977 Pattern recognition in bounded turbulent shear flows. *J. Fluid Mech.* **83**, 673–693.

WEI, T. & WILLMARTH, W. W. 1989 Reynolds-number effects on the structure of a turbulent channel flow. *J. Fluid Mech.* **204**, 57–95.

WILLMARTH, W. W. & BOGAR, T. J. 1977 Survey and new measurements of turbulent structure near the wall. *Phys. Fluids* **20**, S9–S21.

WILLMARTH, W. W. & LU, S. S. 1972 Structure of the Reynolds stress near the wall. *J. Fluid Mech.* **55**, 65–92.

WYNGAARD, J. C. 1969 Spatial resolution of the vorticity meter and other hot-wire arrays. *J. Phys.* E: *Sci. Instrum.* **2**, 983–987.